Journal of The Electrochemical Society, **153** (5) A840-A849 (2006)
0013-4651/2006/153(5)/A840/10/$20.00 © The Electrochemical Society

Stochastic Microstructure Reconstruction and Direct Numerical Simulation of the PEFC Catalyst Layer

Partha P. Mukherjee* and **Chao-Yang Wang****,z**

Electrochemical Engine Center (ECEC) and Department of Mechanical and Nuclear Engineering, The Pennsylvania State University, University Park, Pennsylvania 16802, USA

A direct numerical simulation (DNS) model of species and charge transport in the cathode catalyst layer of a polymer electrolyte fuel cell has been developed. The 3D porous microstructure of the catalyst layer has been reconstructed based on a stochastic technique using the low-order statistical information (porosity, two-point correlation function) as obtained from 2D transmission electron microscopy (TEM) micrographs of a real catalyst layer. In this microscopically complex structure, the DNS model solves point-wise accurate conservation equations, thereby obtaining a pore-scale description of concentration and potential fields. DNS predictions are further compared with the one-dimensional macrohomogeneous results to establish appropriate correlations for effective transport properties as input into macroscopic computational fuel cell models. Finally, the utility of the stochastic reconstruction technique coupled with the DNS model is demonstrated through addressing the influence of microstructural inhomogeneity on the fuel cell performance.
 [DOI: 10.1149/1.2179303]

Manuscript submitted October 18, 2005; revised manuscript received December 29, 2005.
Available electronically March 16, 2006.

In polymer electrolyte fuel cells (PEFCs), electrochemical reactions take place in the catalyst layers (CLs), which are often the thinnest component in a membrane electrode assembly (MEA). Within the anode catalyst layer, hydrogen is oxidized, and within the cathode catalyst layer, oxygen reduction reaction (ORR) takes place to produce water and waste heat. Although there have been tremendous improvements, major voltage losses in PEFCs are still due to poor kinetics of the ORR and mass-transport limitations in the cathode catalyst layer. The cathode catalyst layer is, therefore, a critical component in a PEFC. The catalyst layer has a complex structure, and a good overview of its structure and functions is provided by Gottesfeld and Zawodzinski.[1] For the electrochemical reaction to occur, the cathode catalyst layer must consist of: (*i*) the ionomer, typically fluorinate types such as Nafion, to provide the pathways for proton transport, (*ii*) platinum (Pt) catalysts supported on carbon particles, i.e., the electronic phase for electron conduction, and (*iii*) pores for the oxidant and product water transport.

Different approaches have been undertaken in the literature to model the catalyst layer of a PEFC. In most of the macroscopic models reported in the literature, the active catalyst layer was treated either as an infinitely thin interface or a macrohomogeneous porous layer. A few CL-specific detailed models were developed for PEFCs primarily based on the theory of volume averaging, which can be further distinguished as film model, homogeneous model, and agglomerate model. Several analytical and numerical solutions for the cathode catalyst layer under various conditions were provided by Springer and Gottesfeld,[2] Perry et al.,[3] and Eikerling and Kornyshev.[4] Comprehensive overviews of the various catalyst layer models were furnished in the recent reviews by Wang[5] and Weber and Newman.[6]

Because the catalyst layer consists of both the ionomer and gas phase, water management becomes an important issue, especially for the cathode catalyst layer. The ionomer requires water for good proton conductivity. Water is produced due to ORR, and water also migrates from the anode side through the polymer membrane due to electro-osmotic drag, thus causing flooding of the cathode catalyst layer, leading to hindered oxygen transport to the reaction sites. Hence, investigating water transport in the cathode catalyst layer is of paramount importance. Several groups have modeled water transport in PEFCs at various levels of complexity. Among the various water transport models for the catalyst layer, developed within the general framework of computational fuel cell dynamics (CFCD), notable works include Wang and co-workers,[7,8] Dutta et al.,[9,10] Berning et al.,[11] and Mazumder and Cole.[12] However, as far as the catalyst layer modeling is concerned, Berning et al.[11] treated the catalyst layer as an interface between the membrane and the gas diffusion layer (GDL), Dutta et al.[9,10] did not include the MEA in the computational domain. While Mazumder and Cole[12] supposedly did not consider water transport through the membrane, Wang and co-workers[7,8] provided a comprehensive water transport model throughout the PEFC including the MEA.

However, the above-mentioned macroscopic models do not address localized phenomena at the pore level. Pisani et al.[13] developed an analytical pore-scale model over idealized, one-dimensional pore geometry and assessed the effects of catalyst layer pore structure on polarization performance. In brief, their focus was to distinguish the pore-scale processes (e.g., pore-level variation of reactant concentration in the electrolyte phase) from the ones that do not change over the pore dimension. They derived an analytical expression of a modified Butler–Volmer equation, separately for each simplified geometry under consideration, to describe the effective reaction rate, which, in turn, partly accounts for the porous structure inhomogeneity effect. However, their model lacks the generalized description of pore-scale charge and species transport as well as a realistic CL microstructure. In our recent work,[14,15] a direct numerical simulation (DNS) model has been developed to describe the oxygen and charge transport at the pore level within an idealized as well as a purely random, computer-generated catalyst layer microstructure and the importance of pore-scale modeling of the catalyst layer has been demonstrated.

In the present work, we develop a realistic, statistically rigorous 3D description of the catalyst layer microstructure using a stochastic reconstruction technique with inputs from the transmission electron microscopy (TEM) image of an actual CL and subsequently solve transport equations for charge, oxygen, and water directly at the pore level. We first describe the CL reconstruction using the stochastic generation method. Thereafter, the mathematical description of the DNS model is furnished followed by the discussion of important predictions from this work.

Microstructure Reconstruction

A detail description of the porous microstructure can be obtained in the form of 3D volume data. Several experimental techniques can be deployed to image the pore structure in three dimensions. Earlier attempts include employing destructive serial sectioning of pore casts[16,17] to reconstruct the complex pore space. Recently, noninvasive techniques such as X-ray and magnetic resonance computed microtomography[18,19] and scanning laser confocal microscopy[20] are the preferred choices over the earlier destructive

* Electrochemical Society Student Member.
** Electrochemical Society Active Member.
z E-mail: cxw31@psu.edu

methods. Additionally, 3D porous structure can be generated using stochastic simulation technique, originally developed by Joshi[21] in two dimensions (2D) and later extended to three dimensions (3D) by Quiblier.[22] The stochastic simulation technique is capable of generating 3D replicas of the random microstructure based on specified low-order statistical information (e.g., porosity and two-point correlation function). Such information can be readily obtained from high-resolution 2D binary micrographs of a porous sample. In the absence of adequate 3D volume data, the low cost and high speed of data generation as well as the ability to overcome present resolution constraints of computed microtomography (ca. 5–10 μm per voxel) have established the base for the wide acceptance of the stochastic generation method as a viable alternative to experimental acquisition of 3D volume data.

Stochastic generation method.— The stochastic simulation technique is based on the idea that an arbitrarily complex pore structure can be described by the values of a phase function, $Z(\mathbf{r})$, at each point, $\mathbf{r}$, within the porous medium. The phase function takes the values of zero or unity depending on whether the point corresponds to void or solid, respectively, and can be defined as[23]

$$Z(\mathbf{r}) = \begin{cases} 0 & \text{if } \mathbf{r} \text{ is in the pore space} \\ 1 & \text{otherwise} \end{cases} \quad [1]$$

If the pore structure is statistically homogeneous, then it can be fully, albeit implicitly, described by the first two statistical moments of the binary phase function. These are the porosity ε and two-point autocorrelation function, $R_Z(\mathbf{u})$. The porosity is the probability that a voxel, i.e., each elementary unit arising from discretizing the 3D continuum space, is in the pore space, and is given by[23]

$$\varepsilon = \overline{Z(\mathbf{r})} \quad [2]$$

The two-point autocorrelation function is the probability that two voxels at a distance $\mathbf{r}$ are both in the pore space and can be defined as[23]

$$R_Z(\mathbf{u}) = \overline{[Z(\mathbf{r}) - \varepsilon][Z(\mathbf{r} + \mathbf{u}) - \varepsilon]}/(\varepsilon - \varepsilon^2) \quad [3]$$

where overbar denotes statistical average and $\mathbf{u}$ is the lag vector. For a statistically homogeneous porous medium, ε is a constant and $R_Z(\mathbf{u})$ is only a function of the lag vector, $\mathbf{u}$, i.e., independent of the location vector $\mathbf{r}$. Furthermore, if the porous medium is isotropic, the autocorrelation function $R_Z(\mathbf{u})$ is only a function of the norm of $\mathbf{u}$.

In general, the stochastic generation method creates a realization of the 3D porous medium in terms of a binary, discrete population $Z(x)$, which takes only two values 0 and 1, by transforming a Gaussian set, $X(x)$, of standard, normal variates x. The final 3D binary image represents a porous structure of prescribed porosity and autocorrelation function. As mentioned earlier, this statistics-based reconstruction method was originally developed in 2D by Joshi[21] and extended to 3D by Quiblier.[22] Adler et al.[24] applied it to the reconstruction of Fontainbleau sandstone. Ioannidis et al.[25] modified this method slightly by using discrete Fourier transform, originally devised by Gutjahr.[26] In our study, we employed a simplified version by Bentz and Martys[27] of the approach outlined by Quiblier.[22]

The reconstruction technique starts with computing the autocorrelation function of the 2D TEM image from the original porous medium. To minimize finite size effects, periodic boundaries are utilized during microstructure generation. If the $M \times N$ pixel 2D image is defined as a discrete valued function $I(x,y)$, where $I(x,y)$ is equal to one for solid pixels and zero for pore pixels, the two-point correlation function $S(x,y)$ for the image is given by[28]

$$S(x,y) = \sum_{i=1}^{M} \sum_{j=1}^{N} \frac{I(x,y)^* I(i + x, j + y)}{M^* N} \quad [4]$$

The function $S(x,y)$ is then converted to its polar form $S(r)$ for distances r in pixels by the equation[28]

$$S(r) = \frac{1}{2r + 1} \sum_{l=0}^{2r} S\left(r, \frac{\pi l}{4r}\right) \quad [5]$$

where $S(r) = S(r \cos \theta, r \sin \theta)$ is obtained by bilinear interpolation from the values of $S(x,y)$ determined above.

Following the approach used by Quiblier,[22] the initial reconstructed image consisting of Gaussian distributed noise is generated using a uniform random number generator.[29] The Box–Muller method[30] is used to convert the uniform random deviates to normal deviates. This 3D white noise image, $N(x,y,z)$, is then directly filtered with the autocorrelation function, $F(x,y,z)$, defined as[31]

$$F(r) = F(x,y,z) = \frac{[S(r = \sqrt{x^2 + y^2 + z^2}) - S(0)^* S(0)]}{[S(0) - S(0)^* S(0)]} \quad [6]$$

By definition, $F(0) = 1$ and $F(r) \to 0$ as $r \to \infty$, because $S(r) \to [S(0)]^2$ as $r \to \infty$. The resultant image, $R(x,y,z)$, is then calculated as

$$R(x,y,z) = \sum_{i=0}^{m} \sum_{j=0}^{n} \sum_{k=0}^{p} N(i + x, j + y, k + z)^* F(i,j,k) \quad [7]$$

This method is a simplification of the approach utilized by Quiblier,[22] where a matrix of filtering coefficients is computed by solving a huge system of nonlinear equations and is superior numerically because no inversion is required.

After the filtering process, a gray scale image, $R(x,y,z)$, is obtained. This image is finally converted to a binary (0-pore and 1-solid) image by a thresholding operation. A threshold gray scale is chosen, such that all voxels with gray level above and below this threshold are set to either solid or pore. This threshold gray scale is such that a 3D binary image is created in which the porosity matches that of the original porous medium.

Catalyst layer microstructure.— The cathode catalyst layer consists of a mixture of catalyst platinum supported on carbon, ionomeric electrolyte, and void space. In the present study, the catalyst layer is assumed to contain two phases: the gas phase (i.e., the void space) and a mixed electrolyte/electronic phase (i.e., the solid matrix), henceforth referred to as the electrolyte phase. This assumption will be justified later. Using the aforementioned stochastic reconstruction technique, a 3D description of the catalyst layer microstructure is generated from the 2D TEM image, as shown in Fig. 1a, of an actual catalyst layer. The volume fractions of the constituent phases within the actual catalyst layer are estimated as: pore = 60%, ionomer = 11%, carbon = 27%, and Pt ≅ 2%, based on the methodology described by Gasteiger et al.[32] Briefly, the mass loading data of Pt, carbon, and Nafion is know from the CL fabrication process, respectively, as 0.35 mg Pt/cm^2, 0.525 mg C/cm^2 and 0.22 mg Nafion/cm^2. Now using the bulk density of 2 g/cm^3 for the ionomer and carbon support each and 21.5 g/cm^3 for platinum along with the mass loading data, the volume fraction of each of the constituent phases can be readily calculated for a catalyst layer of thickness 10 μm and the estimates are given above. The two-point autocorrelation function is calculated first from the binarized (pore/solid) 2D image shown in Fig. 1b, generated from the original 2D TEM image, Fig. 1a, using some standard image processing technique. In Fig. 1b, the pore space is white and the solid phase is black. The porosity input for the 3D reconstruction is the actual porosity of the catalyst layer measured a priori using standard techniques. The apparent pore space in the 2D TEM image (Fig. 1b) does not determine porosity but provides the void phase map for determining the two-point autocorrelation function. With this autocorrelation function and a nominal porosity of 0.6 as inputs, the reconstruction simulation model, finally, produces the 3D representation of the catalyst layer and hence the computational domain, as shown in Fig. 2. In order to establish the structural connectivity, the constituent unit cells (void/matrix) within the microstructure are passed through a specialized structural designation routine, as detailed in our earlier

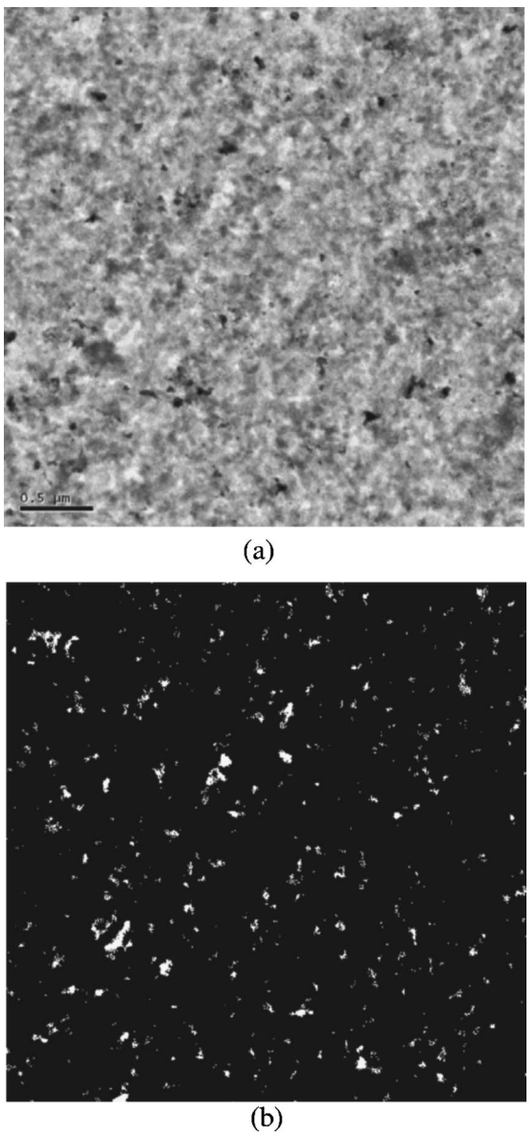

Figure 1. (a) 2D TEM image of the actual catalyst layer and (b) binary (pore/solid) 2D image reduced from the actual TEM image.

work,[15] which identifies the void phase as "transport" and "dead" pore cells and the solid matrix phase as "transport" and "dead" electrolyte cells, respectively. The imposition of the structural identification comes from the fact that the pores, which are connected to each other, form a continuous network, allowing a fluid to transport across the porous medium, henceforth referred to as the "transport" pore cluster. A pore belonging to the "transport" pore cluster is called a "transport" pore; otherwise it is called a "dead" pore. Similar argument applies to the electrolyte phase as well. Figure 3 displays the local distributions of total pore and electrolyte volume fractions across the catalyst layer thickness. Because the porosity is high, the "transport" pore distribution closely follows the total pore distribution, thus leading to a very small "dead" pore volume fraction. Similarly, almost all of the electrolyte phase is "transport" electrolyte. The "electrolyte" phase actually refers to the entire solid matrix in the two-phase reconstruction technique and therefore leads to a relatively large solid matrix fraction. The designation of "transport" and "dead" phase arises strictly from phase-connectivity consideration and follows the underlying stochastic nature of the microstructure reconstructed within the bounds of the specified moments

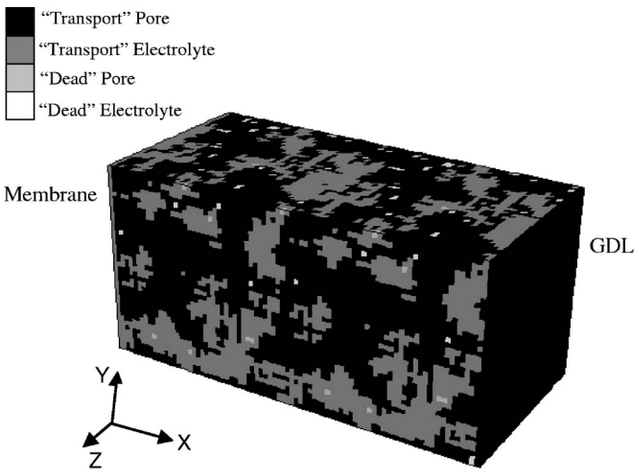

Figure 2. Constructed 3D microstructure of the CL.

of the otherwise random porous structure.[15] The relative distribution of transport and dead phases could be better delineated using a three-phase reconstruction technique consisting of electronic, electrolyte, and void phases, which will be a future extension of the present two-phase reconstruction technique. Protons migrate to the reaction sites through the left boundary, connected to the electrolyte membrane. Oxygen and electrons are transported to the catalyst layer through the right boundary interfacing with the GDL. In the y and z directions, a periodic boundary condition is applied assuming that the actual catalyst layer consists of several repeating units.

DNS Model

Once the microstructure is generated and the constituent phases (i.e., transport and dead pore and electrolyte phases) are identified, point-wise accurate transport equations for charge and species conservation are solved directly on the reconstructed catalyst layer. The meaning of the symbols used in the subsequent sections can be found in the nomenclature.

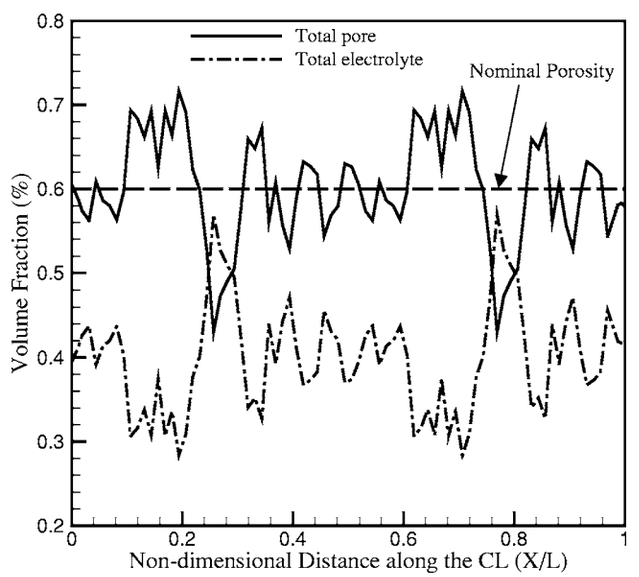

Figure 3. Local pore and electrolyte volume fraction distributions across the thickness of the CL.

Salient physico-electrochemical processes.— The key processes considered in the current DNS model, which describes several interlinked electrochemical and transport phenomena occurring within the catalyst layer, are the following: (*i*) the ORR at the electrochemically active surface, represented by the interface between a "transport" pore and a "transport" electrolyte cell, is given by

$$O_2 + 4H^+ + 4e^- \rightarrow 2H_2O \quad [8]$$

(*ii*) diffusion of oxygen and water vapor through the "transport" pore phase; and (*iii*) charge transport through the "transport" electrolyte phase.

Model assumptions.— The chief assumptions employed in the model are as follows:

1. Isothermal and steady state operation.
2. O_2 diffusion resistance through the polymer electrolyte film covering Pt sites is negligible due to the small thickness of the film ($\sim$5 nm), and thermodynamic equilibrium is assumed to exist at the reaction interface between the oxygen concentration in the gas phase and that dissolved in the electrolyte phase.
3. Because the electrode is very thin and its electronic conductivity is very high, the electronic phase potential is assumed to be uniform and hence, the electron transport is not considered. The ionic conductivity of the mixed phase is thus adjusted using a Bruggeman correction to take into account the effect of the electronic phase volume fraction as follows

$$\kappa = \kappa_0\left(\frac{\varepsilon_e}{\varepsilon_e + \varepsilon_s}\right)^{1.5} = \kappa_0\left(\frac{\varepsilon_e}{1 - \varepsilon_g}\right)^{1.5} \quad [9]$$

where κ_0 is the intrinsic conductivity of the electrolyte, and ε_e, ε_s, and ε_g are the electrolyte, electronic phase, and gas pore volume fractions, respectively;
4. Water is in the gas phase even if the water vapor concentration slightly exceeds the saturation value corresponding to the cell operation temperature (i.e., slight oversaturation is allowed).
5. Water in the electrolyte phase is in equilibrium with the water vapor; thus, only water transport through the gas phase is considered.

Governing equations.— A single set of differential equations valid for all the phases is developed, which obviates the specification of internal boundary conditions at the phase interfaces. Due to slow kinetics of the ORR, the electrochemical reaction is described by the Tafel kinetics as follows

$$j = -i_0\left(\frac{c_{O_2}}{c_{O_2,\mathrm{ref}}}\right)\exp\left(\frac{-\alpha_c F}{RT}\eta\right) \quad [10]$$

where i_0 is the exchange current density, c_{O_2} and $c_{O_2,\mathrm{ref}}$ refer to local oxygen concentration and reference oxygen concentration, respectively, α_c is the cathode transfer coefficient for the ORR, F is Faraday's constant, R is the universal gas constant, and T is the cell operating temperature. A value of 50 nA/cm^2 for the exchange current density is used in the present work. The overpotential, η, is defined as

$$\eta = \phi_s - \phi_e - U_0 \quad [11]$$

where ϕ_s and ϕ_e stand for the electronic and electrolyte phase potentials at the reaction sites, respectively. U_0 is the reference open-circuit potential of the cathode under the cell operation temperature.

The conservation equations for the transport of charge, O_2 and water vapor, respectively, can be expressed as follows

$$\nabla \cdot (\kappa_e \nabla \phi_e) + a\int_\Gamma j\delta(x - x_{\mathrm{interface}})ds = 0 \quad [12]$$

$$\nabla \cdot (D^g_{O_2} \nabla c_{O_2}) + a\int_\Gamma \frac{j}{4F}\delta(x - x_{\mathrm{interface}})ds = 0 \quad [13]$$

$$\nabla \cdot (D^g_{H_2O} \nabla c_{H_2O}) + a\int_\Gamma \frac{j}{2F}\delta(x - x_{\mathrm{interface}})ds = 0 \quad [14]$$

where a represents the specific interfacial area and is defined as the interfacial surface area where the reaction occurs per unit volume of the catalyst layer, s is the nondimensional interface, Γ represents the interfacial surface over which the surface integral is taken, and $\delta(x - x_{\mathrm{interface}})$ is a delta function which is zero everywhere but unity at the interface where the reaction occurs. The second term in the above equations, therefore, represents a source/sink term at the catalyzed interface where the electrochemical reaction takes place. The transfer current density, j, is negative for the electrolyte phase. With a CL thickness of 10 μm, the reconstructed microstructure gives rise to a value of the specific interfacial area, $a = 45 \times 10^5$ m^{-1}, which is an important input to the macrohomogeneous model detailed later.

The above governing equations are extended to be valid for the entire computational domain by introducing a discrete phase function f. The phase function, f, at each elementary cell center (i,j,k), is defined as follows

$$f(i,j,k) = \begin{cases} 0 & \text{"transport" pores} \\ 1 & \text{"transport" electrolytes} \\ 2 & \text{"dead" pores} \\ 3 & \text{"dead" electrolytes} \end{cases} \quad [15]$$

The proton conductivity, oxygen diffusivity, and water vapor diffusivity, respectively, can be correspondingly expressed in terms of the phase function in a discrete fashion as

$$K(i,j,k) = \kappa_e f(i,j,k)[2 - f(i,j,k)][3 - f(i,j,k)]/2 \quad [16]$$

$$D_{O_2}(i,j,k) = D^g_{O_2}[1 - f(i,j,k)][2 - f(i,j,k)][3 - f(i,j,k)]/6 \quad [17]$$

$$D_{H_2O}(i,j,k) = D^g_{H_2O}[1 - f(i,j,k)][2 - f(i,j,k)][3 - f(i,j,k)]/6 \quad [18]$$

The above expressions indicate that the proton conductivity and species diffusivity identically go to zero in the "dead" electrolyte and the "dead" pore cells, respectively.

Now, based on the single-domain approach, the conservation equations, Eq. 12-14 for charge, oxygen, and water transport, respectively, can be discretized using the discrete form of the transport coefficients as well as suitable forms of the source terms. The volumetric source terms for charge, oxygen, and water vapor, S_ϕ, S_{O_2}, and S_{H_2O}, respectively, can be expressed at the cell center (i,j,k), in the discretized form, as

$$\begin{aligned} S_\phi(i,j,k) = -\frac{i_0}{c^g_{O_2,\mathrm{ref}}} f(i,j,k)\exp\left[\frac{\alpha_c F}{RT}\phi_e(i,j,k)\right] \\ \cdot \{[1 - f(i-1,j,k)]c_{O_2}(i-1,j,k)/\Delta x \\ + [1 - f(i+1,j,k)]c_{O_2}(i+1,j,k)/\Delta x \\ + [1 - f(i,j-1,k)]c_{O_2}(i,j-1,k)/\Delta y \\ + [1 - f(i,j+1,k)]c_{O_2}(i,j+1,k)/\Delta y \\ + [1 - f(i,j,k-1)]c_{O_2}(i,j,k-1)/\Delta z \\ + [1 - f(i,j,k+1)]c_{O_2}(i,j,k+1)/\Delta z\} \end{aligned} \quad [19]$$

$$S_{O_2}(i,j,k) = -\frac{i_0}{2Fc^g_{O_2,\mathrm{ref}}}[1-f(i,j,k)]c_{O_2}(i,j,k) \cdot \left\{ f(i-1,j,k)\exp\left[\frac{\alpha_c F}{RT}\phi_e(i-1,j,k)\right]/\Delta x + f(i+1,j,k)\exp\left[\frac{\alpha_c F}{RT}\phi_e(i+1,j,k)\right]/\Delta x + f(i,j-1,k)\exp\left[\frac{\alpha_c F}{RT}\phi_e(i,j-1,k)\right]/\Delta y + f(i,j+1,k)\exp\left[\frac{\alpha_c F}{RT}\phi_e(i,j+1,k)\right]/\Delta y + f(i,j,k-1)\exp\left[\frac{\alpha_c F}{RT}\phi_e(i,j,k-1)\right]/\Delta z + f(i,j,k+1) \times\exp\left[\frac{\alpha_c F}{RT}\phi_e(i,j,k+1)\right]/\Delta z\right\} \quad [20]$$

$$S_{H_2O}(i,j,k) = -\frac{i_0}{4Fc^g_{H_2O,\mathrm{ref}}}[1-f(i,j,k)]c_{H_2O}(i,j,k) \cdot \left\{ f(i-1,j,k)\exp\left[\frac{\alpha_c F}{RT}\phi_e(i-1,j,k)\right]/\Delta x + f(i+1,j,k)\exp\left[\frac{\alpha_c F}{RT}\phi_e(i+1,j,k)\right]/\Delta x + f(i,j-1,k)\exp\left[\frac{\alpha_c F}{RT}\phi_e(i,j-1,k)\right]/\Delta y + f(i,j+1,k)\exp\left[\frac{\alpha_c F}{RT}\phi_e(i,j+1,k)\right]/\Delta y + f(i,j,k-1)\exp\left[\frac{\alpha_c F}{RT}\phi_e(i,j,k-1)\right]/\Delta z + f(i,j,k+1) \times\exp\left[\frac{\alpha_c F}{RT}\phi_e(i,j,k+1)\right]/\Delta z\right\} \quad [21]$$

However, note that the source terms for charge conservation and species conservation exist only in the "transport" electrolyte and "transport" pore cells next to each other, respectively, thus forming an electrochemically active interface.

The transfer current between the two neighboring cells forming an active interface, as shown in Fig. 4, is described by the Tafel equation as follows

$$j = i_0\frac{c_{O_2}(i+1,j,k)}{c^g_{O_2,\mathrm{ref}}}\exp\left[\frac{\alpha_c F}{RT}\phi_e(i,j,k)\right] \ (\mathrm{A/cm^2}) \quad [22]$$

$\phi_e(i,j,k)$ is used to represent the cathode overpotential in the kinetic expression because both the open-circuit potential and the electronic phase potential are constant, and i_0 represents the modified exchange current density after expressing the overpotential, η, in terms of phase potential and open-circuit potential as given by Eq. 11.

Boundary conditions.— For ease of implementation of the boundary conditions, at the left boundary (i.e., the membrane–CL interface), one layer of electrolyte-only cells is added to the computational domain and the operating current is applied uniformly on this layer. Similarly, on the right boundary (i.e., the CL–GDL interface), oxygen and water vapor are supplied at constant concentration on an additional layer of pore-only cells. In the y and z directions, symmetry boundary conditions are applied. To summarize, at $y = 0$, $y = y_L$, $z = 0$, $z = z_L$ at $x = 0$ (i.e., membrane–CL interface), and at $x = x_L$ (i.e., CL–GDL interface), respectively

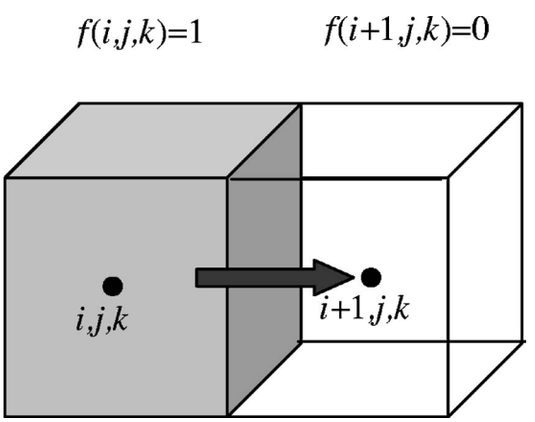

Figure 4. Schematic of the transfer current between two adjacent cells with a catalyzed interface.

$$\frac{\partial c_{O_2}}{\partial n} = 0, \quad \frac{\partial c_{H_2O}}{\partial n} = 0, \quad \frac{\partial \phi_e}{\partial n} = 0 \quad [23]$$

$$\frac{\partial c_{O_2}}{\partial n} = 0, \quad \frac{\partial c_{H_2O}}{\partial n} = -\frac{N_{w,\mathrm{net}}}{D_{H_2O}}, \quad -\kappa\frac{\partial \phi_e}{\partial n} = I \quad [24]$$

$$c_{O_2} = c_{O_2,0}, \quad c_{H_2O} = c_{H_2O,0}, \quad \frac{\partial \phi_e}{\partial n} = 0 \quad [25]$$

The oxygen concentration at the CL–GDL interface is adjusted to take into account the diffusion resistance through the GDL with constant oxygen concentration in the gas channel, thus representative of a physically large stoichiometric flow rate, and is shown in Fig. 5. The oxygen concentration at the CL–GDL interface is given by

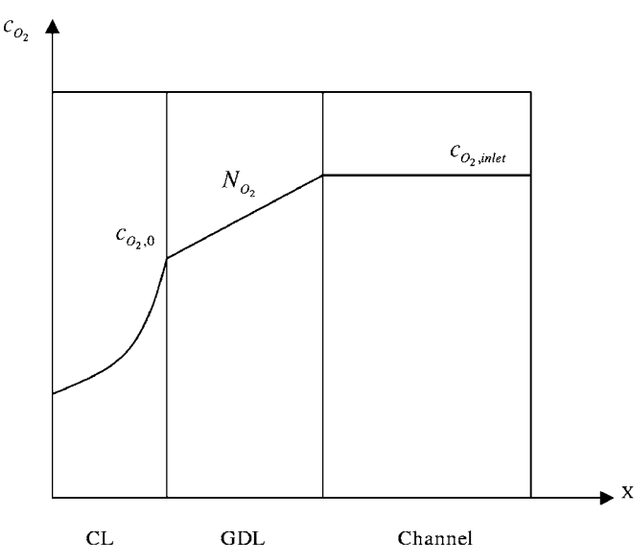

Figure 5. Schematic diagram of the oxygen concentration profile in the cathode.

$$c_{O_2,0} = c_{O_2,\text{inlet}} - \frac{I\Delta X_{GDL}}{4FD^{g,\text{eff}}_{O_2,GDL}} \quad [26]$$

The oxygen concentration profile through the GDL is assumed linear, and $D^{g,\text{eff}}_{O_2,GDL}$ is the effective diffusion coefficient of oxygen adjusted with respect to the GDL porosity, ε_{GDL}, and tortuosity, τ_{GDL}, and is given by

$$D^{g,\text{eff}}_{O_2,GDL} = D^{g}_{O_2}\frac{\varepsilon_{GDL}}{\tau_{GDL}} \quad [27]$$

The evaluation of the effective transport property in the GDL in terms of its porosity and tortuosity is equivalent to the treatment using a Bruggeman-type correlation used elsewhere in this work, because tortuosity is related to porosity, thus essentially leading to a Bruggeman relation.

The boundary conditions for the water vapor transport require special elucidation of the water transport mechanism included in the model. Humidified fuel and oxidant streams are supplied to the fuel cell in order to ensure membrane hydration. Water is transported to the cathode CL from the anode through the membrane by the electro-osmotic drag, expressed by

$$N_{w,\text{drag}} = n_d N_{H^+} = n_d\frac{I}{F} \quad [28]$$

The electro-osmotic drag coefficient, n_d, refers to the number of water molecules migrated across the membrane per proton as current is passed. n_d varies in a wide range depending on the degree of membrane hydration according to the experimental measurements by Zawodzinski et al.[33] In the present study, a constant drag coefficient of unity is used because the water content of interest ranges from zero to 14, corresponding to a partially hydrated membrane. Water is also produced in the cathode CL due to the ORR, which sets in a water concentration gradient resulting in back-diffusion of water from the cathode CL to the anode across the membrane. At higher current densities, the excessive water produced at the cathode is removed via evaporation by the undersaturated oxidant stream.

At the membrane–CL interface, a net water transport coefficient, α, is employed to account for the net water flux across the membrane due to the electro-osmotic drag and back-diffusion effects, and can be expressed as

$$N_{w,\text{net}} = \alpha\frac{I}{F} = N_{w,\text{drag}} - N_{w,\text{dif}} \quad [29]$$

where $N_{w,\text{dif}}$ is the water flux through the membrane due to back-diffusion from the cathode side to the anode side. In the present study, α is assumed to be constant although it depends on the reaction rate and humidity conditions at anode and cathode inlets. A value of $\alpha = 0.2$ is employed for the present study. Thus, the boundary condition at the membrane–CL interface is given by

$$\left.\frac{\partial c_{H_2O}}{\partial x}\right|_{x=0} = -N_{w,\text{net}}/D_{H_2O} \quad [30]$$

At the CL–GDL interface, water vapor concentration is calculated from the concentration of water vapor at the channel inlet with correction for mass-transfer resistance in the GDL and is given by

$$c_{H_2O}|_{x=x_L} = c_{H_2O,\text{inlet}} + N_w|_{x=x_L}\frac{\Delta X_{GDL}}{D^{g,\text{eff}}_{H_2O,GDL}} \quad [31]$$

Similar to the boundary condition treatment for oxygen transport, the water vapor profile in the GDL is assumed linear and the water vapor concentration is constant in the gas channel. The effective diffusion coefficient of water vapor in the gas phase through the GDL is adjusted in a similar fashion as the oxygen diffusion coefficient given by Eq. 20. The water flux through the GDL is the sum of the net flux across the membrane and the water production rate in the catalyst layer and can be expressed as

Table I. Model input parameters for the DNS calculations.

Parameter	Value
Oxygen diffusion coefficient in air, $D^g_{O_2}$ (m^2/s)	9.5×10^{-6}
Water vapor diffusivity in air, $D^g_{H_2O}$ (m^2/s)	1.28×10^{-5}
Oxygen diffusion coefficient in helox, $D^g_{O_2}$ (m^2/s)	2.0×10^{-5}
Water vapor diffusivity in helox, $D^g_{H_2O}$ (m^2/s)	3.3×10^{-5}
Pressure at the gas channel inlet, p (kPa)	200
Operating temperature, T (°C)	70
GDL thickness, ΔX_{GDL} (μm)	290
GDL porosity, ε_{GDL}	0.6
GDL tortuosity, τ_{GDL}	1.5
Nominal porosity of the catalyst layer, ε_g	0.6

$$N_w|_{x=x_L} = N_{w,\text{net}} + N_{w,\text{prod}} = (\alpha + 0.5)\frac{I}{F} \quad [32]$$

From the inlet relative humidity, *RH*, water vapor concentration of the humidified air at the channel inlet is calculated by

$$c_{H_2O,\text{inlet}} = RH \cdot c^{\text{sat}}_{H_2O} \quad [33]$$

where $c^{\text{sat}}_{H_2O}$ is the saturation concentration of water at the cell operating temperature.

Model input parameters.— The operating, geometric, and transport parameters used in the present study are summarized in Table I. However, the physical input parameters for proton conductivity and species diffusivity need special illustration.

Proton conductivity.— The proton conductivity of the electrolyte phase, i.e., Nafion, as a function of water content has been correlated by Springer et al.[34] from experiments as

$$\kappa_0(\lambda) = 100\exp\left[1268\left(\frac{1}{303} - \frac{1}{T}\right)\right](0.005139\lambda - 0.00326)\ (\text{S/m}) \quad [34]$$

where the water content in the membrane, λ, depends on the water activity, a, in the gas phase according to the following experimental data fit

$$\lambda = \begin{cases} 0.043 + 17.81a - 39.85a^2 + 36.0a^3 & \text{for } 0 < a \leqslant 1 \\ 14 + 1.4(a-1) & \text{for } 1 < a \leqslant 3 \end{cases} \quad [35]$$

The water activity, a, is defined as

$$a = \frac{c_{H_2O}}{c^{\text{sat}}_{H_2O}} \quad [36]$$

Substitution of Eq. 35 into Eq. 34 provides the variation of proton conductivity in Nafion with water activity. Thus, the proton conductivity varies at every point within the CL with the variation of water vapor concentration.

Species diffusivity.— The binary diffusion coefficient of species (i.e., oxygen and water vapor), i, in the gas phase depends on temperature and pressure and is given by[35]

$$D^g_{b,i} = D^g_{b,i,0}\left(\frac{T}{T_0}\right)^{3/2}\left(\frac{p_0}{p}\right) \quad [37]$$

In the present study, the reference pressure, p_0, is taken as 1 atm and the reference temperature, T_0, as 273 K. However, for the pore-level DNS modeling in the catalyst layer microstructure, Knudsen diffusion due to molecule-to-wall collision, as opposed to molecule-to-molecule collision in bulk diffusion, becomes important. Therefore, in the present model, a combined diffusivity of species, i, in the gas phase is employed and is given by[5]

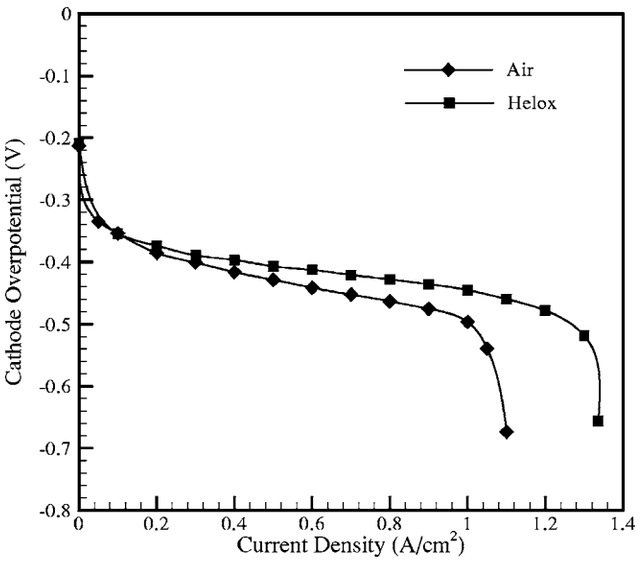

Figure 6. Cathode polarization curves for 100% RH air and helox as oxidants.

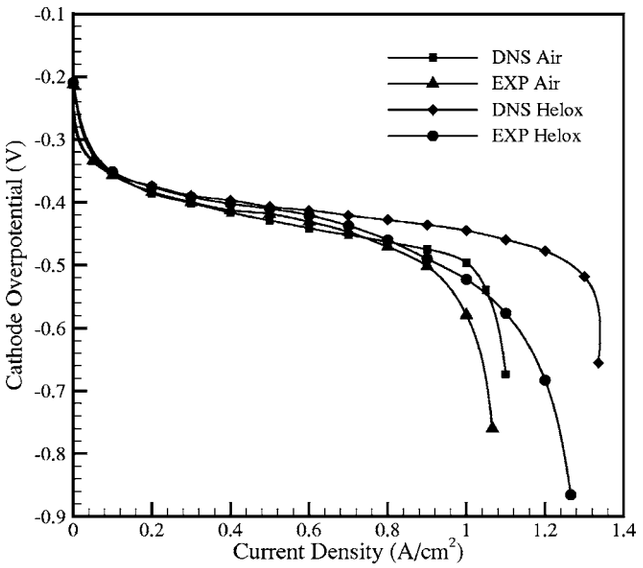

Figure 7. Comparison of the cathode polarization curves between DNS predictions and experimental observations for 100% RH air and helox as oxidants.

$$D_i^g = \left(\frac{1}{D_{b,i}^g} + \frac{1}{D_{K,i}} \right)^{-1} \quad [38]$$

$D_{K,i}$ is the Knudsen diffusion coefficient, which is of the same order of magnitude as the binary diffusion coefficient for the CL, and can be computed according to the kinetic theory of gases as[5]

$$D_{K,i} = \frac{2}{3} \left(\frac{8RT}{\pi M_i} \right)^{1/2} r_p \quad [39]$$

where a representative mean pore radius, r_p, of 50 nm is used in the current model.

Solution procedure.— The conservation equations, Eq. 19-21, are solved using the commercial CFD software Fluent.[36] The user defined function (UDF) capability of Fluent is employed to customize the source terms for modeling the electrochemical reactions at the phase interface as well as to solve the set of governing equations for the DNS model. In the present study, for a ($10 \times 5 \times 5$ μm) CL structure, the number of cells within the computational domain in the x, y, and z directions are $100 \times 50 \times 50$, respectively, leading to an average element (voxel) size of 100 nm, which in turn provides a representative pore size for this model. The reconstruction model with porosity and two-point autocorrelation function as inputs described in this work does not provide a pore size distribution, which however can be achieved with other variants of stochastic reconstruction techniques. Convergence was considered achieved when the relative error between two consecutive iterations reached 10^{-6} for each scalar field. A typical simulation for a particular current density, on a single PC with Pentium 4 processor, 1 GB RAM, 2.79 GHz processor, takes around 8 h.

Results and Discussion

The simulated polarization curves with air and helox (21% O2 and 79% N_2) as the oxidants at 100% inlet humidity with inlet pressure of 200 kPa and cell temperature of 700°C are shown in Fig. 6. The term "polarization curve" refers to the cathode overpotential vs current density curve in the present article and hence differs from the standard I-V curve otherwise used popularly in the fuel cell literature. As a general trend, the predicted cathode polarization curves depict a fast drop in the small current density region controlled by the ORR kinetics followed by a linear voltage drop in the mixed control regime and, finally, at higher current densities (~ 1 A/cm^2), the mass-transport limitation appears with a fast voltage drop resulting from oxygen depletion. Figure 7 shows the comparison of the polarization curves between the DNS predictions and experimental data for air and helox, operated under identical conditions as mentioned earlier. The experimentally obtained cell voltage (V_{cell}) vs current density (I) data was processed to extract the variation of cathode overpotential (η_c) with current density according to the following relation

$$\eta_c = V_{\text{cell}} + I \times HFR - U_0 \quad [40]$$

where *HFR* refers to the high-frequency resistance measured experimentally and U_0 is the thermodynamic equilibrium potential corresponding to the fuel cell operating temperature. In the above equation, the anodic overpotential for hydrogen oxidation and protonic resistance in the anode catalyst layer are assumed to be negligible. However, the cathode overpotential defined in Eq. 40 contains the protonic resistance or ohmic loss in the cathode catalyst layer. From Fig. 7, it is clear that there are reasonable agreements between the DNS predictions and experimental observations in the kinetic-control and ohmic-control regimes. However, both for air and helox, the ohmic-control regime seems to be slightly extended in the DNS calculations. Because water transport has been modeled only in the gas phase, it does not include any water condensation effect and subsequent liquid water motion and might have underpredicted the ohmic-control regime. Also, from the figure it is evident that the cell performance is greatly improved when operated with helox as compared to that with air due to the reduction in the oxygen and water-transport resistances. Higher performance is expected for helox, because oxygen diffusivity is more than two times higher in helox as compared to that in air. Also as expected, with fully humidified helox, DNS calculations predict a higher limiting current density as compared to that with fully humidified air, in accordance with experimental observations. The disagreement between the DNS calculations and experimental data in the transport-control regime could be due to the cathode-only DNS model as opposed to a full fuel cell model, where the mass-transfer resistances through the GDL in both through-plane and in-plane directions are properly modeled. The mass-transport resistance through the GDL was adjusted in the simulations by properly tuning the structural properties, namely, tortuosity, in order to achieve a reasonably realistic limiting current density compared to the experimental data. Nonetheless, Fig. 7 dem-

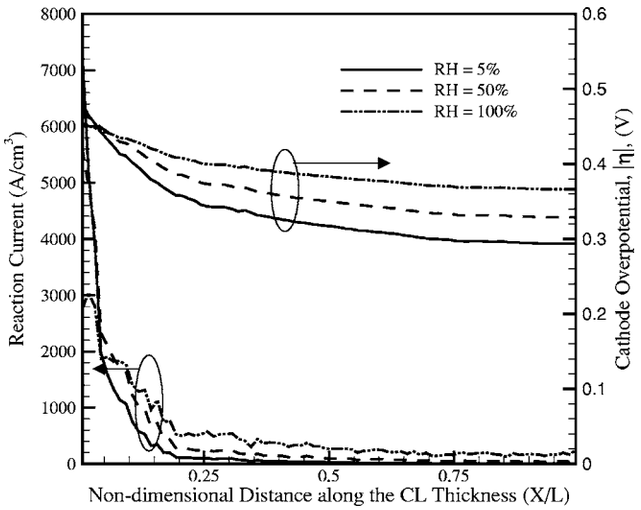

Figure 8. Local overpotential and reaction current density distributions across the thickness of the CL for different inlet humidity with air as the oxidant.

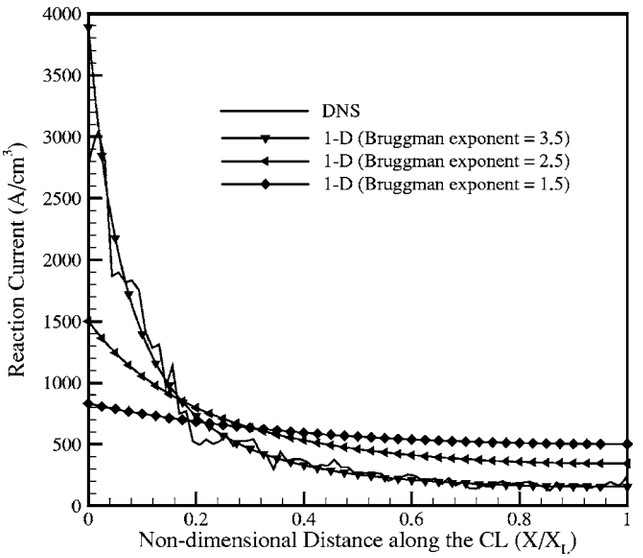

Figure 9. Comparison between the cross-sectional averaged reaction current distributions across the thickness of the CL from the DNS and 1D macrohomogeneous models.

onstrates that the DNS model is not only able of capturing the general trend of the fuel cell performance curve on a realistic CL microstructure but also exhibits sufficient agreement with experimental results.

Figure 8 shows the effect of the inlet humidity on the local cross-section-averaged reaction current and overpotential distributions along the catalyst layer thickness at an average current density of 0.6 A/cm^2 with air as the oxidant. It is clear that the reaction zone shifts toward the membrane–CL interface with lower inlet humidity. Apparently, this is due to the poorer proton conductivity or higher ionic resistance in the electrolyte phase and results in a much lower surface overpotential near the front end of the catalyst layer, i.e., close to the CL–GDL interface. In order to compensate for the lower reaction current produced near the front end of the catalyst layer, the back end, i.e., near the membrane–CL interface, must provide higher reaction current as the average current density is fixed. This leads to a higher surface overpotential needed at the back end of the catalyst layer and hence leads to higher total voltage loss in the cathode for the low-humidity operation.

Comparison of DNS results with 1D macrohomogeneous results.— One major application of the DNS calculation is that we can evaluate the Bruggeman correlation required for the macrohomogeneous models using the DNS data. Details about the macrohomogeneous model can be found in the original work by Springer and co-workers.[2-4] In brief, the governing equations for charge (proton) and species (oxygen and water vapor) transport are solved in the CL domain, which does not contain any microstructural information as in the DNS model but with resistance due to the porous medium structure taken into consideration through effective transport properties. The Bruggeman correction factor, ξ, is commonly applied to determine the effective transport property as follows

$$\Gamma_k^{\text{eff}} = \Gamma_k \varepsilon_k^{\xi} \qquad [41]$$

In the 1D macrohomogeneous model, the same specific surface area, a (cm^2/cm^3), as that in the constructed 3D catalyst layer microstructure is used in the Butler–Volmer equation to represent the volumetric reaction current and is expressed by

$$j = ai_0\left[\exp\left(\frac{\alpha_a F}{RT}\eta\right) - \exp\left(-\frac{\alpha_c F}{RT}\eta\right)\right] \text{ (A/cm}^3\text{)} \qquad [42]$$

Other input parameters for the macrohomogeneous model are rendered the same as in the DNS model for comparison.

Figures 9-11 show the comparison of the cross-section-averaged reaction current, cathode overpotential, and oxygen concentration profiles at an average current density of 0.6 A/cm^2 with air as the oxidant across the CL thickness between the DNS and 1D macrohomogeneous model predictions, respectively. Different Bruggeman factors have been attempted. In the case of the reaction current (Fig. 9) and cathode overpotential (Fig. 10) distributions, the DNS result exhibits good agreement with the 1D macrohomogeneous model prediction with the Bruggeman factor of 3.5. However, Fig. 11 shows that the factor of 4.5 gives a better match for the oxygen concentration profile. The higher value of the Bruggeman correction factor for oxygen concentration could be linked to the higher pore volume fraction ($\varepsilon_g = 0.6$) as opposed to the corresponding electrolyte and electronic phase volume fractions. Related discussions are

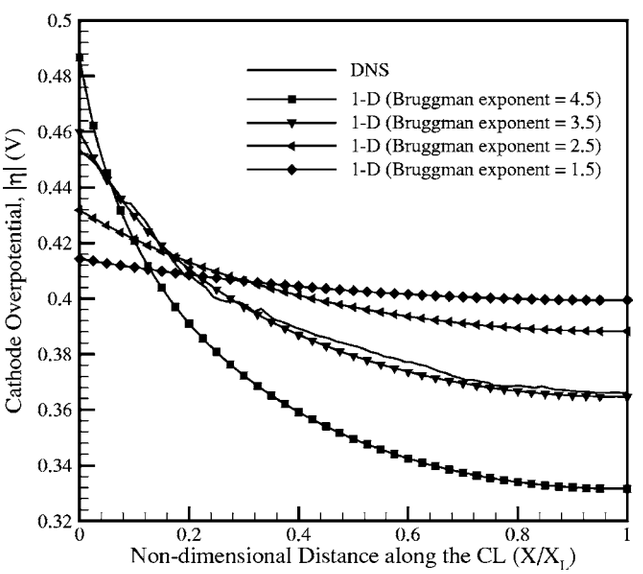

Figure 10. Comparison between the cross-sectional averaged overpotential profiles across the thickness of the CL from the DNS and 1D macrohomogeneous models.

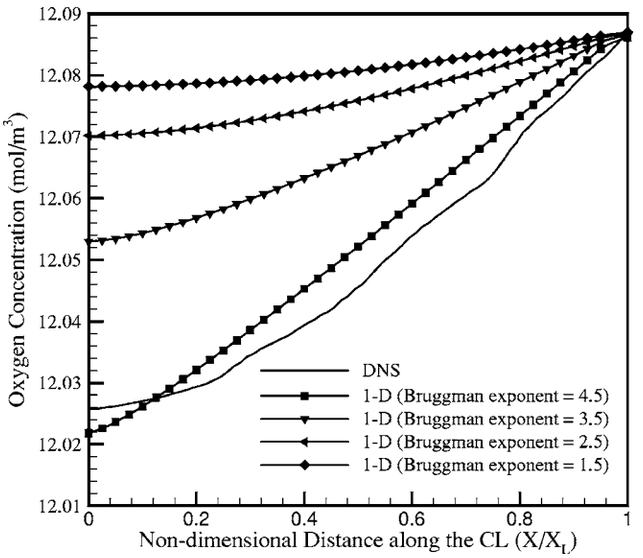

Figure 11. Comparison between the cross-sectional averaged oxygen concentration profiles across the thickness of the CL from the DNS and 1D macrohomogeneous models.

detailed elsewhere.[15] It is also important to note that the high reaction current in the 15–20% of the catalyst layer thickness in the vicinity of the membrane could be attributed to the limited ionomer conductivity resulting from the low electrolyte phase volume fraction ($\sim$11%) throughout the CL. Detailed investigations of the stochastic reconstruction of various actual CLs with different compositions and the effect of the respective microstructure on the cathode performance are presently underway and will be furnished in future communications. Research is also underway to simulate liquid water motion through the complex catalyst layer microstructure at the pore scale, and this liquid water transport process will be further incorporated into the DNS model presented here.

Conclusions

A stochastic reconstruction technique for generation of the cathode catalyst layer microstructure is provided and is integrated seamlessly with the DNS model of species and charge transport, thus providing a comprehensive pore-scale modeling framework. The constructed CL microstructure reflects the statistical nature of the complex porous structure and pointwise accurate conservation equations are solved to describe the underlying transport phenomena. Finally, the predictive capability of the DNS model is demonstrated with the evaluation of the Bruggeman correction factors, which can be used as valuable inputs for the macroscopic fuel cell dynamics models. In addition, the stochastic reconstruction method along with the DNS model could prove to be an effective screening tool for the performance evaluation of the cathode catalyst layers with inputs in terms of an actual TEM image, thus reflecting the interaction of the microstructure with the transport characteristics and hence aiding development of the next generation high-performance CLs.

Acknowledgments

Funding of this work by industrial sponsors of ECEC is gratefully acknowledged. P.P.M. would like to thank D. P. Bentz at the National Institute of Standards and Technology (NIST) for valuable input and discussions during the microstructure reconstruction model development, Dr. X. G. Yang of ECEC for providing the TEM images, and Fuqiang Liu of ECEC for fabricating CL samples and providing the experimental data.

The Pennsylvania State University assisted in meeting the publication costs of this article.

List of Symbols

a	water activity or specific interfacial area, cm^2/cm^3
c_i	local concentration of species I, mol/m^3
D_i	diffusion coefficient of species I, m^2/s
f	phase function for the single domain approach
F	Faraday's constant, 96,487 C/mol
I	current density, A/cm^2
j	reaction current density, A/cm^2
n_d	electro-osmotic drag coefficient
N_i	molar flux of species i, mol/m^2 s
p	pressure, Pa
r_p	mean pore radius, μm
R	universal gas constant, 8.314 J/mol K
RH	relative humidity
R_Z	autocorrelation function
S	source term in the governing equations
T	absolute temperature, K
u_0	thermodynamic equilibrium potential
x	x coordinate, μm
y	y coordinate, μm
z	z coordinate, μm
Z	phase function for the definition of a porous medium

Greek letters

α	net water transport coefficient
α_a	anodic transfer coefficient
α_c	cathodic transfer coefficient
ε_κ	volume fraction of phase, k, in the catalyst layer
η	surface overpotential, V
κ	electrolyte conductivity, S/m
λ	membrane water content, mol H_2O/mol SO_3^-
ϕ_κ	electrical potential in phase k, V
Γ	physicochemical property
ξ	Bruggeman correction factor

Subscripts and superscripts

b	bulk diffusion
e	electrolyte phase
eff	effective
g	gas phase
GDL	gas diffusion layer
inlet	gas channel inlet
K	Knudsen diffusion
L	catalyst layer thickness
net	net value
O_2	oxygen
prod	water production in the cathode catalyst layer
ref	reference value
s	solid phase
sat	saturation of water
w	water
0	boundary value at the CL–GDL interface or initial/intrinsic value

References

1. S. Gottesfeld and T. A. Zawodzinski, in *Advances in Electrochemical Science and Engineering*, Vol. 5, C. Tobias, Editor, Wiley and Sons, New York (1997).
2. T. E. Springer and S. Gottesfeld, in *Modeling of Batteries and Fuel Cells*, R. E. White, M. W. Verbrugge, and J. F. Stockel, Editors, PV 91–10, p. 197, The Electrochemical Society Proceedings Series, Pennington, NJ (1991).
3. M. L. Perry, J. Newman, and E. J. Cairns, *J. Electrochem. Soc.*, **145**, 5 (1998).
4. M. Eikerling and A. A. Kornyshev, *J. Electroanal. Chem.*, **453**, 89 (1998).
5. C. Y. Wang, *Chem. Rev. (Washington, D.C.)*, **104**, 4727 (2004).
6. A. Z. Weber and J. Newman, *Chem. Rev. (Washington, D.C.)*, **104**, 4679 (2004).
7. S. Um, C. Y. Wang, and K. S. Chen, *J. Electrochem. Soc.*, **147**, 4485 (2000).
8. S. Um and C. Y. Wang, *J. Power Sources*, **125**, 40 (2004).
9. S. Dutta, S. Shimpalee, and J. W. Van Zee, *J. Appl. Electrochem.*, **30**, 135 (2000).
10. S. Dutta, S. Shimpalee, and J. W. Van Zee, *Int. J. Heat Mass Transfer*, **44**, 2029 (2001).
11. T. Berning, D. M. Lu, and N. Djilali, *J. Power Sources*, **106**, 284 (2002).
12. S. Mazumder and J. V. Cole, *J. Electrochem. Soc.*, **150**, A1503 (2003).
13. L. Pisani, M. Valentini, and G. Murgia, *J. Electrochem. Soc.*, **150**, A1558 (2003).
14. G. Wang, P. P. Mukherjee, and C. Y. Wang, *Electrochim. Acta*, In press (2005), electronic copy available at Elsevier website.
15. G. Wang, P. P. Mukherjee, and C. Y. Wang, *Electrochim. Acta*, In press (2005), electronic copy available on Elsevier website.
16. M. J. Kwiecien, I. F. Macdonald, and F. A. L. Dullien, *J. Microsc.*, **159**, 343 (1990).
17. D. P. Lymberopoulos and A. C. Payatakes, *J. Colloid Interface Sci.*, **150**, 61 (1992).
18. P. Spanne, J. F. Thovert, J. C. Jacquin, W. B. Lindquist, K. W. Jones, and P. M.

Adler, *Phys. Rev. Lett.*, **73**, 2001 (1994).
19. C. A. Baldwin, A. J. Sederman, M. D. Mantle, P. Alexander, and L. F. Gladden, *J. Colloid Interface Sci.*, **181**, 79 (1996).
20. J. T. Fredrich, B. Menendez, and T. F. Wong, *Science*, **268**, 276 (1995).
21. M. Joshi, Ph.D. Dissertation, University of Kansas, Lawrence, KS (1974).
22. J. A. Quiblier, *J. Colloid Interface Sci.*, **98**, 84 (1984).
23. P. M. Adler, *Porous Media: Geometry and Transports*, Butterworth-Heinemann, Stoneham, MA (1992).
24. P. M. Adler, C. G. Jacquin, and J. A. Quiblier, *Int. J. Multiphase Flow*, **16**, 691 (1990).
25. M. Ioannidis, M. Kwiecien, and I. Chatzis, *SPE Petroleum Computer Conference*, Houston, TX, June 11–14, 1995.
26. A. L. Gutjahr, Project Report, New Mexico Institute of Mining and Technology, Contract no. 4-R58–2690R (1989).
27. D. P. Bentz and N. S. Martys, *Transp. Porous Media*, **17**, 221 (1995).
28. J. G. Berryman, *J. Appl. Phys.*, **57**, 2374 (1985).
29. W. H. Press and S. A. Teukolsky, *Comput. Phys.*, **6**, 522 (1992).
30. A. M. Law and W. D. Kelton, *Simulation Modeling and Analysis*, McGraw-Hill, New York (1982).
31. N. Cressie, *Statistics for Spatial Data*, John Wiley & Sons, New York (1991).
32. H. A. Gasteiger, W. Gu, R. Makharia, M. F. Mathias, and B. Sompalli, in *Handbook of Fuel Cells—Fundamentals, Technology and Applications*, W. Vielstich, A. Lamm, and H. A. Gasteiger, Editor, Chap. 46, Vol. 3, Wiley, Chichester (2003).
33. T. A. Zawodzinski, J. Davey, J. Valerio, and S. Gottesfeld, *Electrochim. Acta*, **40**, 297 (1995).
34. T. E. Springer, T. A. Zawodzinski, and S. Gottesfeld, *J. Electrochem. Soc.*, **138**, 2334 (1991).
35. R. B. Bird, W. E. Stewart, and E. N. Lightfoot, *Transport Phenomena*, 2nd ed., Wiley, New York (2002).
36. Fluent 6.1 UDF Manual, Fluent, Inc., NH, USA.